




Article

Multilevel Dual Active Bridge Leakage Inductance Selection for Various DC-Link Voltage Spans

Babak Khanzadeh ^{1,*} , Torbjörn Thiringer ¹  and Mohammad Kharezy ^{1,2} ¹ Division of Electric Power Engineering, Chalmers University of Technology, 412 96 Göteborg, Sweden² RISE Research Institutes of Sweden, Brinellgatan 4, 501 15 Borås, Sweden

* Correspondence: ababak@chalmers.se

Abstract: The leakage inductance of the transformer in a dual active bridge (DAB) dc–dc converter directly impacts the ac current waveforms and the power factor; thus, it can be considered a design requirement for the transformer. In the existing literature, a choice is made to either ensure soft switching in nominal power or to minimize the RMS current of the transformer. The inductance is typically obtained using optimization procedures. Implementing these optimizations is time-consuming, which can be avoided if a closed-form equation is derived for the optimum leakage inductance. In this paper, analytical formulas are derived to estimate the desired leakage inductance such that the highest RMS value of the current in the operation region of a DAB is kept to its minimum value. The accuracy and sensitivity of the analytical solutions are evaluated. It is shown that in a large design domain, the solution for the YY-connected MFT has a less than 3% error compared to the results obtained from an optimization engine. As an example of the importance of selecting the leakage inductance correctly, it is shown that for 11% deviations in the dc link voltages, a 10% deviation from the desired leakage inductance value can cause 2% higher RMS currents in the converter.

Keywords: dc–dc power conversion; dual active bridge (DAB); modular multilevel converter (MMC); leakage inductance; optimization



Citation: Khanzadeh, B.; Thiringer, T.; Kharezy, M. Multilevel Dual Active Bridge Leakage Inductance Selection for Various DC-Link Voltage Spans. *Energies* **2023**, *16*, 859. <https://doi.org/10.3390/en16020859>

Academic Editors: Julio Cesar Rosas Caro, Jonathan C. Mayo-Maldonado and Jesús Elias Valdez Resendiz

Received: 19 December 2022

Revised: 3 January 2023

Accepted: 10 January 2023

Published: 11 January 2023



Copyright: © 2023 by the authors. Licensee MDPI, Basel, Switzerland. This article is an open access article distributed under the terms and conditions of the Creative Commons Attribution (CC BY) license (<https://creativecommons.org/licenses/by/4.0/>).

1. Introduction

A dual active bridge (DAB) dc–dc converter is formed by two active bridges connected in a front-to-front configuration with a transformer in between [1]. As the ac-link is confined between two inverters, the fundamental frequency can be increased. The increase in the frequency reduces the size of the transformer, which is then referred to as a medium-frequency transformer (MFT). The MFT provides galvanic isolation between the primary and the secondary side dc-links. This makes the DAB suitable for applications like dc offshore wind farms and high-power traction where galvanic isolation and a high voltage transformation ratio are system requirements [2,3]. The conventional DAB is suitable for low-voltage applications. However, it requires a serial connection of semiconductors for higher voltages. This makes it unsuitable for medium- and high-voltage applications [4,5]. For these voltages, multilevel converter topologies are more suitable [2,6–11].

Two important factors in the design of a DAB converter are power density and efficiency. The power density can be improved drastically by reducing the size of passive components like the transformer and capacitors (in the case of a multilevel converter). The size of capacitors can be reduced by selecting the modulation technique (e.g., quasi-two-level (Q2L) modulation [10,11]); selecting the transformer winding connection [12]; and selecting the converter topology [13]. On the other hand, the MFT is not an off-the-shelf product and should be designed for the specific application to have high power density and efficiency. The design optimization of the MFT can be combined with the converter design [14] or performed stand-alone with the specifications imposed from the converter side [15–22].

The MFT's leakage inductance directly impacts the current waveforms, the power factor, and the converter's performance [1]. Therefore, it can be considered to be a design requirement for MFT optimization [15–26]. The value of desired leakage inductance is used as an input for the optimization of an MFT in [15–20]. Its value is selected such that all of the switches achieve turn-on ZVS at the nominal power of the converter for a given deviation from the nominal dc-link voltages [16,17]. This method is suitable for applications where the switching losses make up a substantial part of the converter's losses.

If the leakage inductance is selected inappropriately, a small deviation in the dc-link voltages will give huge reactive currents through the converter [23,24,27]. This is important in designing multilevel converters, as the submodule capacitors should be overrated to handle excessive currents. It also is crucial in applications where conduction losses are the main loss component and variable dc-link voltages are required. The required dc-link voltage ranges change based on the application and characteristics of the connected loads or sources. In automotive applications, the deviations from the nominal point can be up to 34% [28,29]. In [14], a DAB with a wide input range of 100–700 V (75% deviation) is studied for microgrid applications. Therefore, it is important to select the inductance such that the RMS currents (thus, the copper losses) are kept to a minimum in the whole operating range.

In [30], leakage inductance optimization of a 1ϕ conventional DAB is studied for vehicular applications. The phase shift between the two bridges, the leakage inductance, and the dc conversion ratio are swept to find an optimum value of the leakage inductance that minimizes the RMS current. A similar approach is taken in [31] to select the optimum leakage inductance of a 3ϕ multilevel DAB for wind turbine applications. A brute-force optimization method is used in [30,31], which is computationally demanding and time-consuming.

A leakage inductance optimization methodology is presented in [27] for a 3ϕ conventional DAB and utility applications. It uses the analytical power and current formulas of the 3ϕ DAB with a numerical solver to find the optimum value. Even though the method used in [27] gives the optimum leakage inductance value faster than the brute-force method used in [30,31], it does not provide a holistic view of the dependency of the leakage inductance on the design parameters. Moreover, if the topologies of the inverters are altered, the method should be adapted to the new topology.

An interesting approach is taken in [23] for a 1ϕ DAB. A closed-form formula is derived for the desired leakage inductance, which results in the minimum RMS current for a given variation in the dc-link voltage. This is the fastest method possible that also gives a holistic view of the dependency of the leakage inductance on the converter parameters. Optimized designs with this method can be found in [25,26]. Nevertheless, [23] only considers a variation in one of the dc-link voltages and can not be used for applications where both dc-link voltages are variable.

Missing in the available literature is a closed-form equation that provides satisfactory results for the desired leakage inductance of a 1ϕ and 3ϕ MFT that results in the minimum RMS current for arbitrary variations in both dc-link voltages. This paper provides closed-form formulas to calculate the optimum leakage inductance of a two- or multilevel DAB dc–dc converter for both 1ϕ and 3ϕ variants. The accuracy of such a formula is evaluated, and the impact of voltage spans on the RMS currents and the leakage inductance is studied. Additionally, the effect of neglecting the ac resistance of the MFT on the optimization results is quantified.

2. AC-Link Current and Voltage Derivations

Figure 1 shows the topology of a DAB dc–dc converter with a 3ϕ MFT. In this paper, YY, $\Delta\Delta$, and Y Δ winding configurations are considered and studied. As can be seen, the nodes of the primary and secondary sides are marked with capital and lowercase letters, respectively.

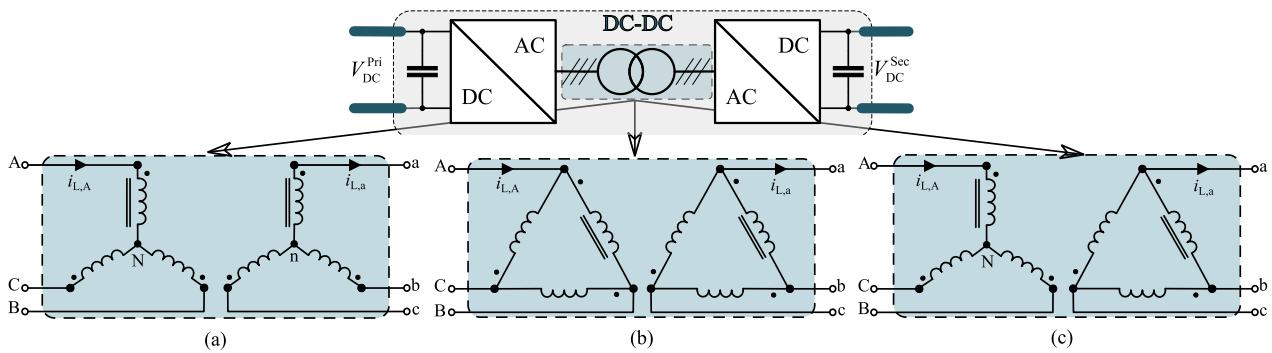


Figure 1. Topology of a 3φ DAB dc-dc converter with different transformer winding configurations. (a) YY configuration. (b) ΔΔ configuration. (c) YΔ configuration.

Figure 2 shows the phase-to-ground (phase to mid-point of the dc-link) voltage waveforms of a multilevel DAB converter. The waveforms of this figure are used as a reference for later derivations in the article. This approach is taken to derive equations independent of the converter’s topologies and the winding configuration. One can modify the final equations accordingly to obtain relationships with the physical parameters of the inverters (as an example, the parameter U in Figure 2 is equivalent to the submodule voltage of an MMC converter).

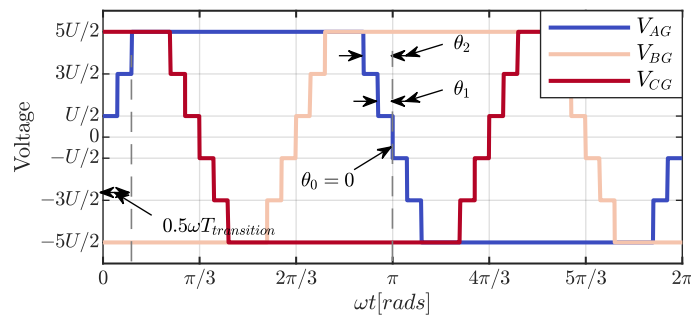


Figure 2. Phase-to-ground voltage waveforms of a 3φ multilevel DAB converter.

2.1. AC-Link Voltages of the 3φ DAB

It is assumed that the 3φ system is balanced. Therefore, only phase A is analyzed hereafter. Using the Fourier series [11,32], the phase-to-ground (P2G) voltages (v_{xG} , $x \in \{A,B,C\}$) can be calculated as

$$v_{xG} = \sum_{H=1}^{\infty} \left(\frac{4U_{H,p}}{H\pi} \sin(H(\omega t + \alpha)) \right), \quad \alpha \in \{0, -2\pi/3, 2\pi/3\} \quad (1)$$

where $\omega = 2\pi f_{sw}$, f_{sw} is the switching frequency, and $U_{H,m}$ is defined as

$$U_{H,m} \equiv U_{H,m}(M_m, U_m, \theta_{k,m}) \triangleq \sum_{k=0}^{M_m-1} (1 - 0.5\delta_j(\theta_{k,m})) U_m \cos(H\theta_{k,m}) \quad (2)$$

where $H \in \{2h - 1 | h \in \mathbb{N}\}$ is the harmonic order, U is the amplitude of each level in the voltage waveform (see Figure 2), δ_j is Kronecker delta [33] (not to be confused with Dirac delta), M is the number of levels in the P2G voltage (defined as the number of steps from $V = 0$ to the peak of the voltage waveform), and θ_k is the duration of each level as depicted in Figure 2. Moreover, $m \in \{p, s\}$, where p refers to the primary bridge parameters and s refers to the secondary bridge parameters. In some multilevel converters, the amplitude of the first step (for $\theta_0 = 0$) is half of the others. To account for this, the Kronecker delta is included in (2). If it is not the case, the term $0.5\delta_j(\theta_k)$ must be excluded from (2). As an example, the conventional DAB does not have this characteristic, therefore, $0.5\delta_j(\theta_k) \equiv 0$.

Phase A voltage of a Y-connected winding, v_{AN} , can be calculated as [34]

$$v_{AN} = v_{AG} - \frac{v_{AG} + v_{BG} + v_{CG}}{3} = \sum_{H=1}^{\infty} \left(\frac{4U_{H,p}}{H\pi} \sin(H\omega t) \right) \tag{3}$$

where $H \in \{2h - 1 | h \in \mathbb{N}, 3 \nmid 2h - 1\}$. Similarly, phase A voltage of a Δ -connected winding, v_{AB} , can be derived as [34]

$$v_{AB} = v_{AG} - v_{BG} = \sum_{H=1}^{\infty} \left(\frac{4U_{H,p}}{H\pi} \left(\sin(H\omega t) - \sin\left(H\omega t - \frac{2H\pi}{3}\right) \right) \right) \tag{4}$$

where $H \in \{2h - 1 | h \in \mathbb{N}, 3 \nmid 2h - 1\}$.

2.2. AC-Link Currents for a YY-Connected 3 ϕ MFT

The primary side phase A current of a YY-connected MFT, I_{LA} , can be calculated as

$$I_{LA}(\omega t) = \sum_{H=1}^{\infty} \frac{4U_{H,p}}{\pi H |Z_H|} \sin(H\omega t - \angle Z_H) - \sum_{H=1}^{\infty} \frac{4N_p U_{H,s}}{\pi N_s H |Z_H|} \sin(H(\omega t - \varphi) - \angle Z_H) \tag{5}$$

where $H \in \{2h - 1 | h \in \mathbb{N}, 3 \nmid 2h - 1\}$, Z is the series impedance of the MFT, φ is the phase-shift between the primary side and the secondary side voltages, N_p is the number of turns of the primary winding, and N_s is the number of turns of the secondary winding. Moreover,

$$\begin{aligned} |Z_H| &= \sqrt{R^2 + (H\omega L_\sigma)^2} \\ \angle Z_H &= \tan^{-1}(H\omega L_\sigma / R_{ac}) \end{aligned} \tag{6}$$

where L_σ and R_{ac} are the primary-side-referred leakage inductance and ac resistance of the transformer, respectively. The RMS of the current in (5) can be calculated as

$$I_{LA}^{RMS} = \sqrt{8 \sum_{H=1}^{\infty} \frac{U_{H,p}^2 + \left(\frac{N_p U_{H,s}}{N_s}\right)^2 - \frac{2N_p U_{H,p} U_{H,s}}{N_s} \cos(H\varphi)}{\pi^2 H^2 |Z_H|^2}} \tag{7}$$

and the active power of the converter, $\bar{P}_{3\phi}$, can be calculated as

$$\bar{P}_{3\phi} = \sum_{H=1}^{\infty} \frac{24U_{H,p}}{\pi^2 H^2 |Z_H|} \left(U_{H,p} \cos(\angle Z_H) - \frac{N_p U_{H,s}}{N_s} \cos(H\varphi + \angle Z_H) \right). \tag{8}$$

Figure 3 shows the dependency of $\sin(\angle Z_H)$ and $\cos(\angle Z_H)$ on the ratio of ωL_σ to R_{ac} . With an increase in $\omega L_\sigma / R_{ac}$, the value of $\sin(\angle Z_H)$ quickly approaches unity. The rate of decrease of $\cos(\angle Z_H)$ is much lower compared with $\sin(\angle Z_H)$, and for $\omega L_\sigma / R_{ac} \geq 50$, it can be approximated to be zero.

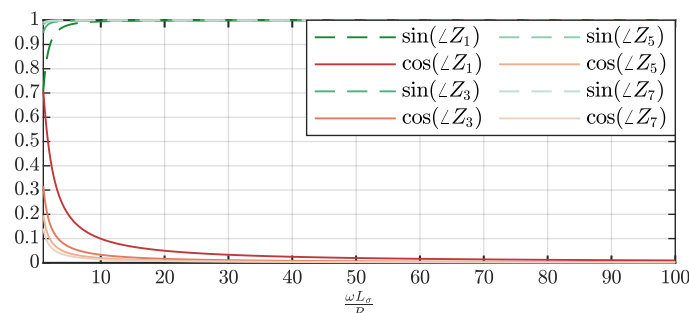


Figure 3. Dependencies of $\sin(\angle Z_H)$ and $\cos(\angle Z_H)$ on the ratio of ωL_σ to R for four harmonics.

Therefore, MFT’s impedance can be approximated with the leakage inductance, assuming $\omega L_\sigma / R_{ac} \geq 50$. Considering this, (7) can be approximated with

$$I_{LA}^{RMS} \approx \sqrt{8 \sum_{H=1}^{\infty} \frac{U_{H,p}^2 + \left(\frac{N_p U_{H,s}}{N_s}\right)^2 - \frac{2N_p U_{H,p} U_{H,s}}{N_s} \cos(H\varphi)}{(\pi\omega L_\sigma)^2 H^4}} \tag{9}$$

and (8) can be rewritten as

$$\bar{P}_{3\phi} \approx \frac{24N_p}{N_s \pi^2 \omega L_\sigma} \sum_{H=1}^{\infty} \left(\frac{U_{H,p} U_{H,s}}{H^3} \sin(H\varphi) \right). \tag{10}$$

2.3. AC-Link Currents for a ΔΔ-Connected 3φ MFT

By defining $L_\sigma^{\Delta\Delta} \triangleq 3L_\sigma$ and applying the Y-Δ transformation to the equivalent circuit of the ΔΔ-connected MFT, one can get the same equivalent circuit as the YY-connected MFT. Consequently, (9) and (10) can also be used to model a ΔΔ-connected MFT. Therefore, only a YY-connected MFT is analyzed hereafter.

2.4. AC-Link Currents for a YΔ-Connected 3φ MFT

If $\omega L_\sigma / R_{ac}$ is large enough, the RMS value of the primary side phase A current, I_{LA} , can be calculated as

$$I_{LA}^{RMS} \approx \sqrt{8 \sum_{H=1}^{\infty} \frac{U_{H,p}^2 + 3\left(\frac{N_p U_{H,s}}{N_s}\right)^2 - \frac{4N_p U_{H,p} U_{H,s}}{N_s} \sin\left(\frac{H\pi}{3}\right) \sin\left(\frac{H\pi}{2}\right) \cos(H\varphi)}{(\pi\omega L_\sigma)^2 H^4}} \tag{11}$$

where $H \in \{2h - 1 | h \in \mathbb{N}, 3 \nmid 2h - 1\}$. Moreover, the transmitted active power can be calculated as

$$\bar{P}_{3\phi} \approx \frac{48N_p}{N_s \pi^2 \omega L_\sigma} \sum_{H=1}^{\infty} \frac{U_{H,p} U_{H,s}}{H^3} \sin\left(\frac{H\pi}{3}\right) \sin\left(\frac{H\pi}{2}\right) \sin(H\varphi) \tag{12}$$

2.5. AC-Link Voltages and Currents for a 1φ MFT

The Fourier series of the phase voltage of a 1φ multilevel DAB converter, v_φ , can be written as

$$v_\varphi = v_{AG}(\omega t) - v_{AG}(\omega t - \pi) = \sum_{H=1}^{\infty} \left(\frac{8U_{H,p}}{H\pi} \sin(H\omega t) \right) \tag{13}$$

where $H \in \{2h - 1 | h \in \mathbb{N}\}$. If $\omega L_\sigma / R_{ac}$ is large enough, then the RMS value of the primary side phase current, $I_{L\varphi}^{RMS}$, can be approximated as

$$I_{L\varphi}^{RMS} \approx \sqrt{\sum_{H=1}^{\infty} \frac{U_{H,p}^2 + \left(\frac{N_p U_{H,s}}{N_s}\right)^2 - \frac{2N_p U_{H,p} U_{H,s}}{N_s} \cos(H\varphi)}{(\pi\omega L_\sigma / \sqrt{32})^2 H^4}}. \tag{14}$$

where $H \in \{2h - 1 | h \in \mathbb{N}\}$. Also, the active power, $\bar{P}_{1\phi}$, can be approximated as

$$\bar{P}_{1\phi} = \frac{32N_p}{N_s \pi^2 \omega L_\sigma} \sum_{H=1}^{\infty} \left(\frac{U_{H,p} U_{H,s}}{H^3} \sin(H\varphi) \right). \tag{15}$$

It is important to note that for a 1φ DAB converter, all the odd harmonics are present in the phase current and voltage waveforms.

3. Study of the Leakage Inductance

Figure 4 depicts the dependency of the RMS currents of a 3 ϕ DAB, I_{RMS} , on the leakage inductance for different percentages of deviation from the primary nominal dc-link voltage, σ_{pri} , while the active power is kept constant at its nominal value. As can be seen, for the operation with fixed dc-link voltage, the smaller the value of L_σ , the lower the value of I_{RMS} . Moreover, for any $L_\sigma \in (0, 0.6)$ pu, the converter can transfer the nominal power without a large increase in the RMS value of the current. However, for the slightest deviation in the dc-link voltage, huge currents are required to transfer the nominal power if L_σ is below 0.1 pu. Similarly, if L_σ is too large (e.g., larger than 0.6 pu for $\sigma_{pri} < -40\%$), the converter must be derated, as the maximum phase shift, φ , is the limiting factor.

For the case shown in Figure 4, L_σ can be easily selected because deviations exist only on one of the dc-links. As an example, if a deviation of a maximum 30% is expected on the primary side dc-link voltage, the selection of $L_\sigma = 0.5$ pu will ensure that the currents will be kept below one pu (as shown in Figure 4). Finding an optimum L_σ becomes more complicated for the cases where deviations higher and lower than the nominal dc-link voltage exist on both sides. Therefore, it is necessary to formulate an optimization problem to find the optimum leakage inductance value.

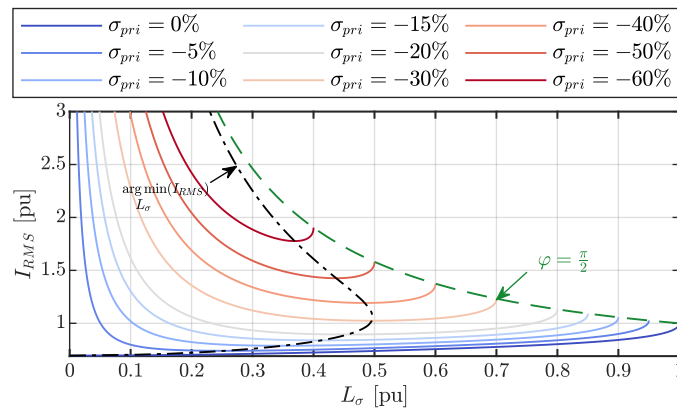


Figure 4. Dependency of the RMS value of the phase currents on the leakage inductance for different percentages of deviation in the primary side nominal dc-link voltage, σ_{pri} , while the active power is kept constant at its nominal value.

3.1. Formulating the Optimization

Let us assume the converter’s primary and secondary side voltages have variations in a range of $U_{pN}[(1 - \sigma_{p1}), (1 + \sigma_{p2})]$ and $U_{sN}[(1 - \sigma_{s1}), (1 + \sigma_{s2})]$, respectively; where U_{pN} and U_{sN} are the nominal values of U_p and U_s ; and σ_{p1} and σ_{p2} are the percentages of deviation in the primary dc-link voltage. Similarly, σ_{s1} and σ_{s2} are the percentages of deviation in the secondary dc-link voltage.

The operation region of the converter is illustrated with a gray-shaded area in Figure 5. This rectangular domain, \mathcal{R}_d , can be formulated as

$$\left| \frac{U_p - U_{pM}}{\sigma_p U_{pM}} + \frac{U_s - U_{sM}}{\sigma_s U_{sM}} \right| + \left| \frac{U_p - U_{pM}}{\sigma_p U_{pM}} - \frac{U_s - U_{sM}}{\sigma_s U_{sM}} \right| \leq 2. \tag{16}$$

where (U_{pM}, U_{sM}) is the center of the rectangular domain and σ_p and σ_s are the deviations from the center given as

$$\begin{cases} U_{pM} = \frac{U_{pN}}{2} (2 + \sigma_{p2} - \sigma_{p1}) \\ U_{sM} = \frac{U_{sN}}{2} (2 + \sigma_{s2} - \sigma_{s1}) \end{cases}, \quad \begin{cases} \sigma_p = \frac{\sigma_{p2} + \sigma_{p1}}{2 + \sigma_{p2} - \sigma_{p1}} \\ \sigma_s = \frac{\sigma_{s2} + \sigma_{s1}}{2 + \sigma_{s2} - \sigma_{s1}} \end{cases}. \tag{17}$$

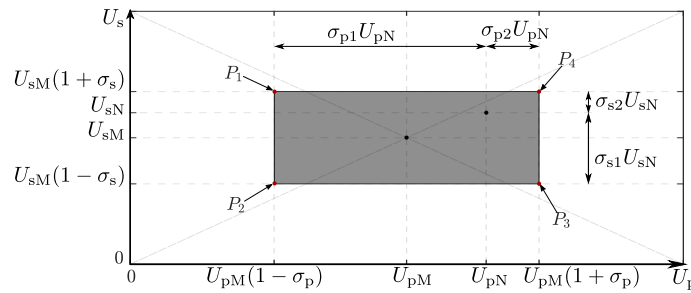


Figure 5. The operation region of the converter with the nominal point shown by (U_{pN}, U_{sN}) .

The aim is to find a leakage inductance value that minimizes the RMS currents in the operation domain \mathcal{R}_d while transferring the nominal power of the converter, P_n . Therefore the optimization can be formulated as

$$\begin{aligned} & \arg \min_{L_\sigma \in \mathbb{R}^+} \left(\max_{U_p, U_s} \left(I_{LA}^{\text{RMS}} \right) \right) \\ & \text{subject to: } (U_p, U_s) \in \mathcal{R}_d, \\ & \quad \bar{P}_{3\phi} = P_n. \end{aligned} \tag{18}$$

3.2. Leakage Inductance Calculation for the 3φ Topology

Solving (18) analytically becomes impossible if all of the harmonics are considered. However, a first harmonic approximation can be used since the current and power are inversely proportional to H^4 and H^3 , respectively. The first harmonic approximation for the YY connection results in

$$I_{LA,1}^{\text{RMS}} \approx \sqrt{8} \frac{\sqrt{U_{1,p}^2 + \left(\frac{N_p U_{1,s}}{N_s}\right)^2} - \sqrt{\left(\frac{2N_p U_{1,p} U_{1,s}}{N_s}\right)^2 - \left(\frac{\pi^2 \omega L_\sigma P_n}{12}\right)^2}}{\pi \omega L_\sigma}. \tag{19}$$

For the YΔ, it yields

$$I_{LA,1}^{\text{RMS}} \approx \sqrt{8} \frac{\sqrt{U_{1,p}^2 + \left(\frac{\sqrt{3} N_p U_{1,s}}{N_s}\right)^2} - \sqrt{\left(\frac{2\sqrt{3} N_p U_{1,p} U_{1,s}}{N_s}\right)^2 - \left(\frac{\pi^2 \omega L_\sigma P_n}{12}\right)^2}}{\pi \omega L_\sigma}. \tag{20}$$

Therefore, (18) can be simplified as

$$\begin{aligned} & \arg \min_{L_\sigma \in \mathbb{R}^+} \left(\max_{U_p, U_s} \left(I_{LA,1}^{\text{RMS}} \right) \right) \\ & \text{subject to: } (U_p, U_s) \in \mathcal{R}_d. \end{aligned} \tag{21}$$

The process of solving (21) is provided in Appendix A. Using the following definitions

$$U_{1,p,M} \stackrel{\triangle}{=} U_{1,p}(M_p, U_{pM}, \theta_{k,p}) \text{ and } U_{1,s,M} \stackrel{\triangle}{=} \frac{N_p U_{1,s}(M_s, U_{sM}, \theta_{k,s})}{N_s} \text{ for YY} \tag{22a}$$

$$U_{1,p,M} \stackrel{\triangle}{=} U_{1,p}(M_p, U_{pM}, \theta_{k,p}) \text{ and } U_{1,s,M} \stackrel{\triangle}{=} \frac{\sqrt{3} N_p U_{1,s}(M_s, U_{sM}, \theta_{k,s})}{N_s} \text{ for Y}\Delta \tag{22b}$$

assuming that $U_{1,p,M} \approx U_{1,s,M}$. The solution of (21) is given as

$$L_{\sigma,opt} = \frac{24U_{1,p,M}^2}{\pi^2\omega P_n} \times G_{L\sigma} \tag{23}$$

where $G_{L\sigma}$ is a gain, defined as

$$G_{L\sigma} = \begin{cases} \mathcal{G}_{L\sigma}(\sigma_s, \sigma_p) & \forall (\sigma_p, \sigma_s) \in \mathcal{I} \\ \mathcal{G}_{L\sigma}(\sigma_p, \sigma_s) & \forall (\sigma_p, \sigma_s) \in \mathcal{J} \end{cases} \tag{24}$$

and $\mathcal{G}_{L\sigma}(\sigma_1, \sigma_2) = \sqrt{\sigma_1}\sqrt{2 - \sigma_1}\sqrt{1 - 2\sigma_1 + \sigma_1^2 - \sigma_2^2}$. The subsets \mathcal{I} and \mathcal{J} are defined as

$$\mathcal{I} = \{(\sigma_p, \sigma_s) \mid 0 \leq \sigma_p, \sigma_p \leq \sigma_s, \sigma_p + \sigma_s \leq 1, \sigma_s + \sqrt{\sigma_p} \leq 1\} \tag{25a}$$

$$\mathcal{J} = \{(\sigma_p, \sigma_s) \mid 0 \leq \sigma_s, \sigma_s \leq \sigma_p, \sigma_p + \sigma_s \leq 1, \sigma_p + \sqrt{\sigma_s} \leq 1\}. \tag{25b}$$

By analyzing $\mathcal{G}_{L\sigma}$, one can see that σ_2^2 can be neglected compared to the other terms for small values of σ_1 . Therefore, $L_{\sigma,opt}$ depends mainly on σ_1 if σ_1 is small. However, the term σ_2^2 can not be neglected for large values of σ_1 . Therefore, $L_{\sigma,opt}$ will have a dependency on both σ_1 and σ_2 for large values of σ_1 .

Figure 6a illustrates the value of $G_{L\sigma}$ as a function of σ_p and σ_s . The sets \mathcal{I} and \mathcal{J} are depicted with green and orange dashed lines, respectively. There is symmetry in the value of $G_{L\sigma}$ along the identity line ($\sigma_p = \sigma_s$). A zoomed version of Figure 6a is depicted in Figure 6b. In this region, the iso-lines are almost parallel with the axes, meaning that $G_{L\sigma}$ and consequently $L_{\sigma,opt}$ depend mainly on $\max(\sigma_p, \sigma_s)$.

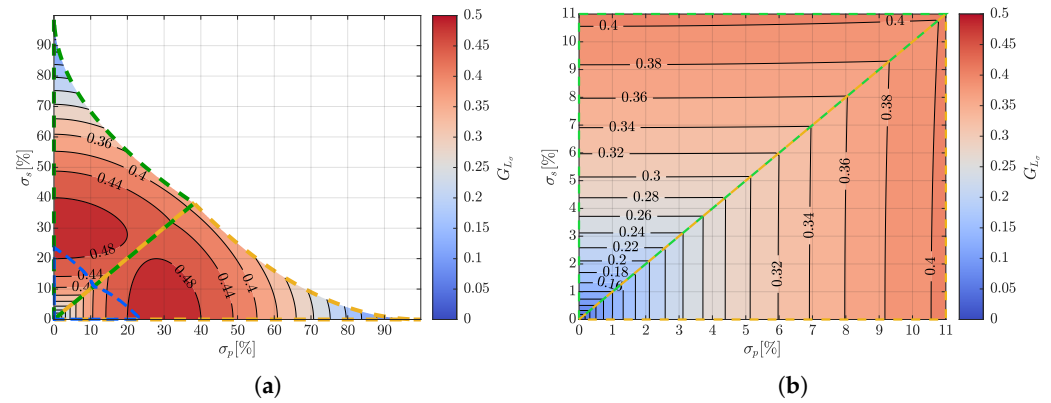


Figure 6. Visualization of $G_{L\sigma}$ given in (24). The triangle with green dashed lines corresponds to the set \mathcal{I} given in (25a), and the one with orange dashed lines corresponds to the set \mathcal{J} given in (25b). (a) For $\sigma_p \leq 100\%$ and $\sigma_s \leq 100\%$. (b) For $\sigma_p \leq 11\%$ and $\sigma_s \leq 11\%$.

For applications with a high switching frequency, the switching losses are also detrimental to the efficiency of the converter. The dashed blue lines in Figure 6a show the boundaries of the soft-switching region. For the voltage deviations inside this region, the selection of the leakage inductance from (23) also ensures soft-switching in the whole \mathcal{R}_d . As shown in [11], the soft-switching range drifts toward large phase shifts with an increase in the transition time. Therefore, the region marked with the dashed blue line will shrink for non-zero transition time values and eventually disappear.

3.3. Leakage Inductance Calculation for 1 ϕ Topology

Unlike the 3 ϕ topology, the third harmonic also contributes to the power transfer in the 1 ϕ variant. However, its contribution to the power transfer is, approximately, 27 times

less than the contribution of the fundamental harmonic. Therefore, similar assumptions as for the 3ϕ variant can be made for the calculation of $L_{\sigma,opt}$, which results in

$$L_{\sigma,opt} = \frac{32U_{1,p,M}^2}{\pi^2\omega P_n} \times G_{L\sigma} \tag{26}$$

where P_n is the nominal power of the 1ϕ converter. Finally, for clarification, Figure 7 shows a flowchart of the optimum leakage inductance calculation process.

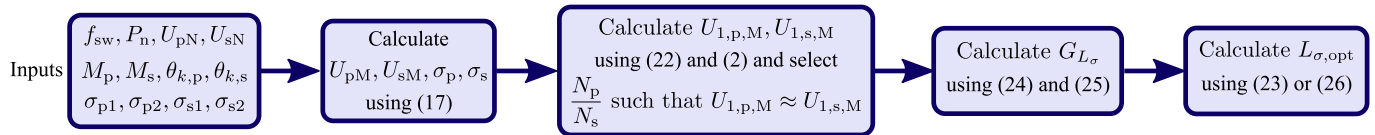


Figure 7. Optimum leakage inductance calculation flowchart.

3.4. Sensitivity Analysis

The presence of harmonics transmitting active power will affect the value of $L_{\sigma,opt}$. It is essential to investigate the sensitivity of the current to changes in the leakage inductance value to validate the relations derived earlier. The deviation in the $L_{\sigma,opt}$ value, $\delta_{L_{\sigma,opt}}$, is defined as

$$\delta_{L_{\sigma,opt}} = \frac{\Delta L_{\sigma,opt}}{L_{\sigma,opt}} = \frac{L_{\sigma,non-opt} - L_{\sigma,opt}}{L_{\sigma,opt}} \Rightarrow L_{\sigma,non-opt} = (1 + \delta_{L_{\sigma,opt}})L_{\sigma,opt} \tag{27}$$

where $L_{\sigma,non-opt}$ is the non-optimum value of the leakage inductance. Similarly, the deviation in the RMS value of the current, $\delta_{I_{LA,1}^{RMS}}$, is defined as

$$\delta_{I_{LA,1}^{RMS}} = \frac{\left| I_{LA,1}^{RMS} \Big|_{L_{\sigma,non-opt}} - I_{LA,1}^{RMS} \Big|_{L_{\sigma,opt}} \right|}{I_{LA,1}^{RMS} \Big|_{L_{\sigma,opt}}} \times 100\%. \tag{28}$$

Figure 8 shows the value of $\delta_{I_{LA,1}^{RMS}}$ for the points with the maximum current in the operation region when $\delta_{L_{\sigma,opt}} = \pm 2.5\%$. The maximum current occurs on points P_1 or P_3 for $\delta_{L_{\sigma,opt}} = -2.5\%$. For these points, $\delta_{I_{LA,1}^{RMS}}$ is below 2%, as shown in Figure 8a. Similarly, Figure 8b shows $\delta_{I_{LA,1}^{RMS}}$ for the point with maximum current when $\delta_{L_{\sigma,opt}} = 2.5\%$ (i.e., point P_2). Similar to the $\delta_{L_{\sigma,opt}} = -2.5\%$ case, the deviation stays below 2% for most (σ_p, σ_s) pairs. However, for certain (σ_p, σ_s) pairs, the deviation increases dramatically and even becomes a complex value (where iso-lines disappear). In that region, the phase shift between the primary side and the secondary side bridges is close to 90 degrees. Therefore, the converter will lose the capability to transmit the full power at point P_2 for a small change in L_{σ} . Additionally, for large values of ϕ , $dI_{LA,1}^{RMS}/dL_{\sigma}$ increases quickly (see Figure A1 in Appendix A). Therefore, a small deviation in $L_{\sigma,opt}$ will result in a large deviation in the RMS value of the current.

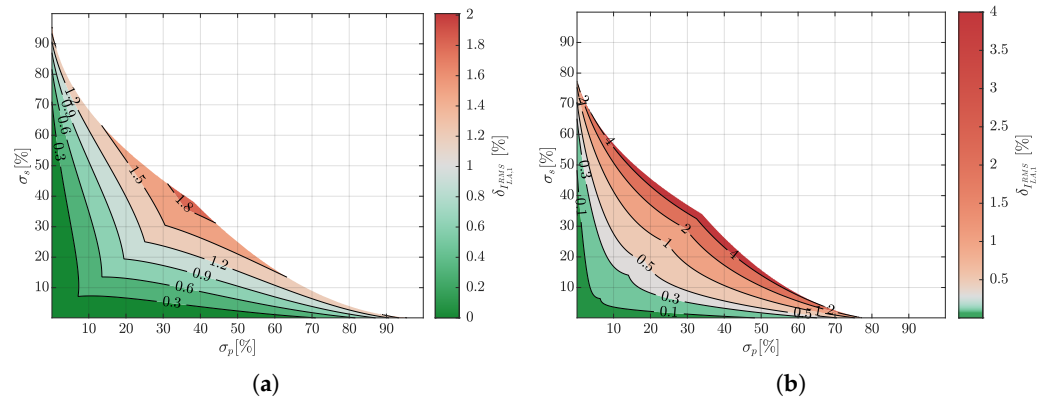


Figure 8. $\delta_{L\sigma,\text{opt}}^{\text{RMS}}$ for different σ_p and σ_s values. (a) For $\delta_{L\sigma,\text{opt}} = -2.5\%$ on points P_1 or P_3 . (b) For $\delta_{L\sigma,\text{opt}} = 2.5\%$ on point P_2 .

4. Simulation and Verification

An analytical expression is derived for $L_{\sigma,\text{opt}}$ in the previous section, and sensitivity analysis is performed. However, these are done assuming that the ac resistance of the MFT and the harmonics can be neglected. A simulation model is developed to investigate the validity of these assumptions and to verify the analytical model.

4.1. L_{σ} Calculation Using Simulation Models

MATLAB models that emulate the behavior of 1ϕ and 3ϕ multilevel DAB dc–dc converters are developed. The converters are assumed to have the same power and dc-link voltage ratings. The rated power is assumed to be 2 MW, and both dc-link voltages are assumed to be 5 kV. The modular-multilevel converter (MMC) topology is used for the primary side and the secondary side inverters. The number of sub-modules per arm, N_{SM} , is selected to be five. The MMC with five sub-modules can produce a P2G voltage waveform with five levels using either the complementary or the non-complementary switching sequence [11]. It is assumed that the converter has a switching frequency of 5 kHz and that the dwell time, t_{dwell} , (the time spent on each level of the trapezoidal waveform before a new sub-module is inserted or bypassed) is 2.5 μs . Therefore, the percentage of total transition times per fundamental period ($2f_{\text{sw}}T_{\text{transition}}$) is 10%. Table 1 summarizes the specifications of the simulated converter.

Table 1. Specifications of the simulated dc–dc converters.

Parameter	Value	Parameter	Value	Parameter	Value	Parameter	Value
$V_{\text{dc,nom}}^{\text{Pri}}$	5 kV	f_{sw}	5 kHz	$V_{\text{dc,nom}}^{\text{Sec}}$	5 kV	P_{nom}	2 MW
σ_p	[0.02, 0.35]	N_{SM}	5	σ_s	[0.02, 0.35]	t_{dwell}	2.5 μs

The series ac resistance is neglected for this simulation, and the method explained in [31] is used to obtain the desired leakage inductance of the 3ϕ MFT. A similar approach is taken for the 1ϕ case. Figure 9 shows the leakage inductance requirements of the 3ϕ and the 1ϕ MFTs obtained from the simulations. As can be seen, they have similar patterns as Figure 6a. However, $L_{\sigma,\text{opt}}$ of the 1ϕ MFT is larger than that of the 3ϕ variants, which is due to higher winding voltages of the 1ϕ MFT.

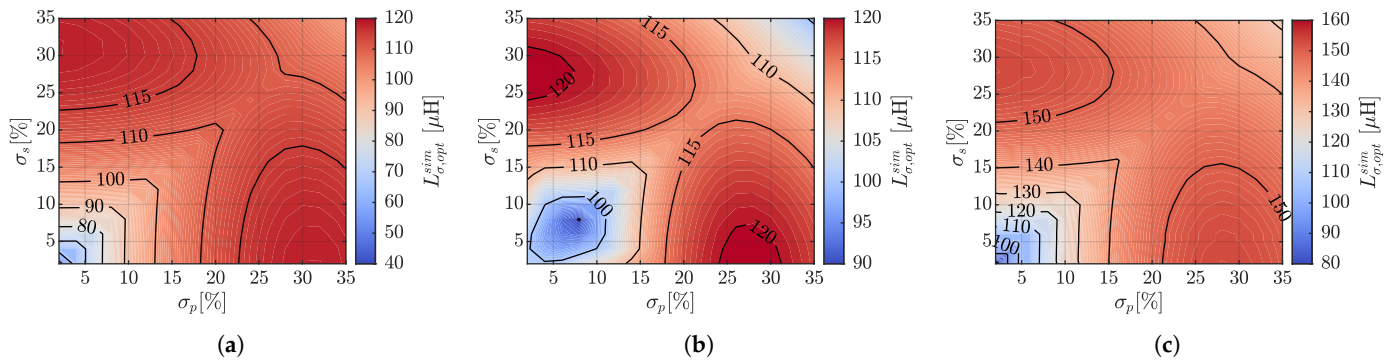


Figure 9. Numerical solution for $L_{\sigma,opt}$ with the converter specifications given in Table 1. (a) For the 3 ϕ YY-connected MFT. (b) For the 3 ϕ Y Δ -connected MFT. (c) For the 1 ϕ MFT.

4.2. L_{σ} Calculation Using Simulation Models

For an MMC with 5 sub-modules and dc-link voltages of 5 kV, U_{pN} and U_{sN} are equal to 1 kV. Moreover, σ_{p2} and σ_{p1} are assumed to be equal (similarly, $\sigma_{s2} = \sigma_{s1}$). Using (17), one can obtain $\sigma_p = \sigma_{p2} = \sigma_{p1}$, $\sigma_s = \sigma_{s2} = \sigma_{s1}$, and $U_{pM} = U_{pN} = U_{sN} = U_{sM}$. Additionally, $\theta_k = 2k\pi f_{sw} T_{dwell}$ for $k \in \{0, 1, 2\}$, and

$$U_{1,p,M} = U_{1,s,M} = \left(0.5 + \sum_{k=1}^2 \cos(2k\pi f_{sw} T_{dwell}) \right) \text{kV}. \quad (29)$$

Eventually, (23)–(26) can be used to calculate $L_{\sigma,opt}$. Figure 10 shows the percentage of error in the estimation of the leakage inductance from (23)–(26), which is defined as

$$L_{\sigma,opt}^{error} = \frac{L_{\sigma,opt}^{sim} - L_{\sigma,opt}^{calc}}{L_{\sigma,opt}^{sim}} \times 100\% \quad (30)$$

where $L_{\sigma,opt}^{sim}$ is the value obtained from the simulations (shown in Figure 9) and $L_{\sigma,opt}^{calc}$ is the value obtained from the analytical formulas (23)–(26). As can be seen, for most of the region, $L_{\sigma,opt}^{error}$ is below 2.5% and 4% for the YY-connected 3 ϕ and the 1 ϕ cases, respectively. A higher error is expected for the 1 ϕ case, as the third harmonic also contributes to power transfer, which is neglected in the calculations. $L_{\sigma,opt}^{error}$ increases for the Y Δ case when deviations in the dc-links are below 10%. This is because the lower the deviations in the dc-links, the lower the phase shift obtained from L_{σ} optimization. The fifth and seventh harmonics are the dominant components of the current for low phase shift and the Δ Y configuration as shown in [35]. This makes the first harmonic approximation invalid for the Δ Y configuration and low phase shift values. Thus, the solution obtained from the analytical calculations has a higher error in this region.

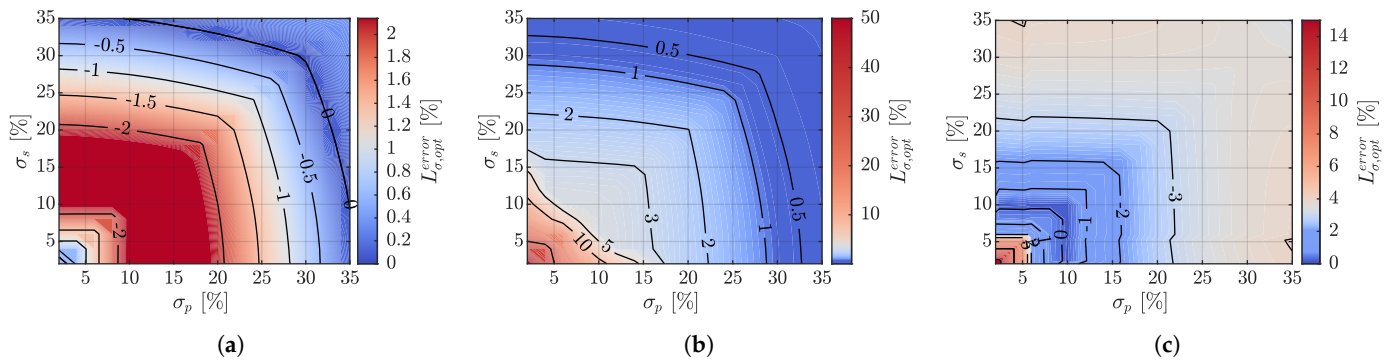


Figure 10. The percentage of error in the estimation $L_{\sigma, opt}$, using analytical formulas (23)–(26), for the dc–dc converter with the given specifications in Table 1. (a) For the 3ϕ YY-connected MFT. (b) For the 3ϕ Y Δ -connected MFT. (c) For the 1ϕ MFT.

Figure 11a shows $L_{\sigma, opt}^{error}$ of the YY-connected 3ϕ MFT for three different percentages of the total transition times per fundamental period. For $\sigma_p \leq 2\%$ or $\sigma_s \leq 2\%$, the estimation error increases dramatically. However, for the rest of the region, $L_{\sigma, opt}^{error}$ is below 3%. For a given (σ_p, σ_s) , an increase in $2f_{sw}T_{transition}$ reduces the estimation error. This is because the THD of the phase current reduces with higher transition times and, accordingly, the accuracy of the first harmonic approximation increases.

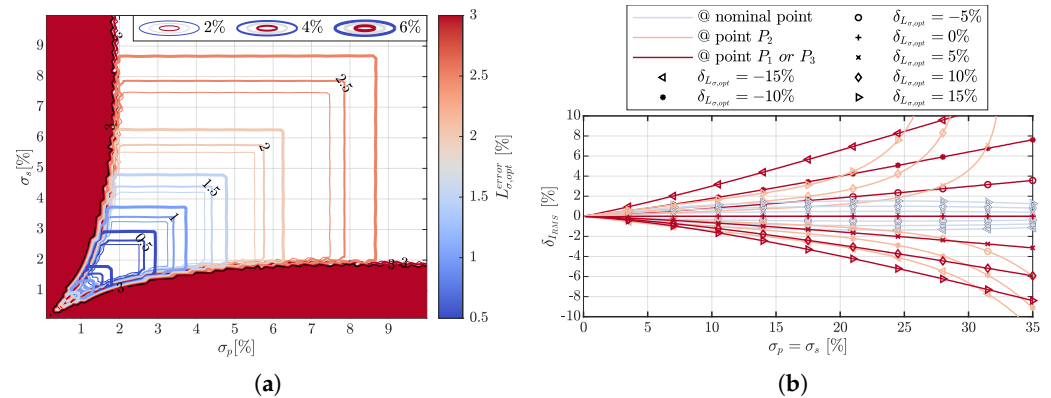


Figure 11. (a) $L_{\sigma, opt}^{error}$ of the YY-connected 3ϕ MFT for different percentages of total transition times per fundamental period ($2f_{sw}T_{transition}$). In the red-colored region, the error is higher than 3%. (b) The deviation in the RMS value of the phase current for a 3ϕ YY-connected DAB at the nominal power for different percentages of deviation from the desired leakage inductance obtained from (23).

Figure 11b visualizes the deviation in the RMS value of the phase current for a 3ϕ YY-connected DAB at the nominal power for different percentages of deviation from the desired leakage inductance obtained from (23). When the converter operates with nominal voltages, $\delta_{I_{RMS}}$ is larger than zero for any $\delta_{L_{\sigma, opt}} > 0$. The maximum value of $\delta_{I_{RMS}}$ occurs at $\sigma_p = \sigma_s \approx 23\%$, which is below 1% for $\delta_{L_{\sigma, opt}} < 10\%$. The larger the $|\delta_{L_{\sigma, opt}}|$, the higher the $|\delta_{I_{RMS}}|$. The effect is more pronounced when the converter operates at non-nominal points—specifically at points P_i , $i \in \{1, 2, 3\}$. For these points, the higher the $\sigma_p = \sigma_s$, the higher the $|\delta_{I_{RMS}}|$. For example, a 10% deviation from the desired leakage inductance value can cause 2% higher RMS currents at points P_1 or P_3 in the converter for $\sigma_p = \sigma_s = 11\%$. For large enough $\sigma_p = \sigma_s$, even a 5% deviation from $L_{\sigma, opt}$ can cause more than 5% higher currents in the converter. Therefore, it is important to choose the leakage inductance value as close to the value given by (23) as possible to avoid extra losses and derating of the converter.

4.3. Sensitivity Study on R_{ac}

To calculate the phase currents of the MFT, the series ac resistance is neglected in Section 2 provided that $\omega L_{\sigma}/R_{ac}$ is large. Measurements conducted on two MFT prototypes and simulations presented in this section will be used to justify this assumption. The leakage inductance and the ac resistance are measured on two shell-type MFT prototypes, one with ferrite and the other with nanocrystalline cores. The MFTs are rated for 50 kW, 5 kHz, and 1 kV to 3 kV. More information on the design methodology of MFTs can be found in [17,36].

The leakage inductance and the ac resistance are measured from the secondary side while the primary side is short-circuited, as shown in Figure 12a. The measurements are performed in the frequency range of 1 kHz to 40 kHz using an Agilent E4980A RLC meter. Figure 12b shows the measured leakage inductance and ac resistance of both MFTs. The ratio of the leakage reactance to the ac resistance is calculated from these measurements and is shown in Figure 12c. For the fundamental component and operation with 5 kHz, the ratio is 51 and 43 for ferrite and nanocrystalline MFTs, respectively. The ratio is above 80 for transformers and the 3rd, 5th, and 7th harmonics. This justifies the assumption made in Section 2.2 for the dominant harmonics (i.e., $\omega L_{\sigma}/R_{ac} \geq 50$).

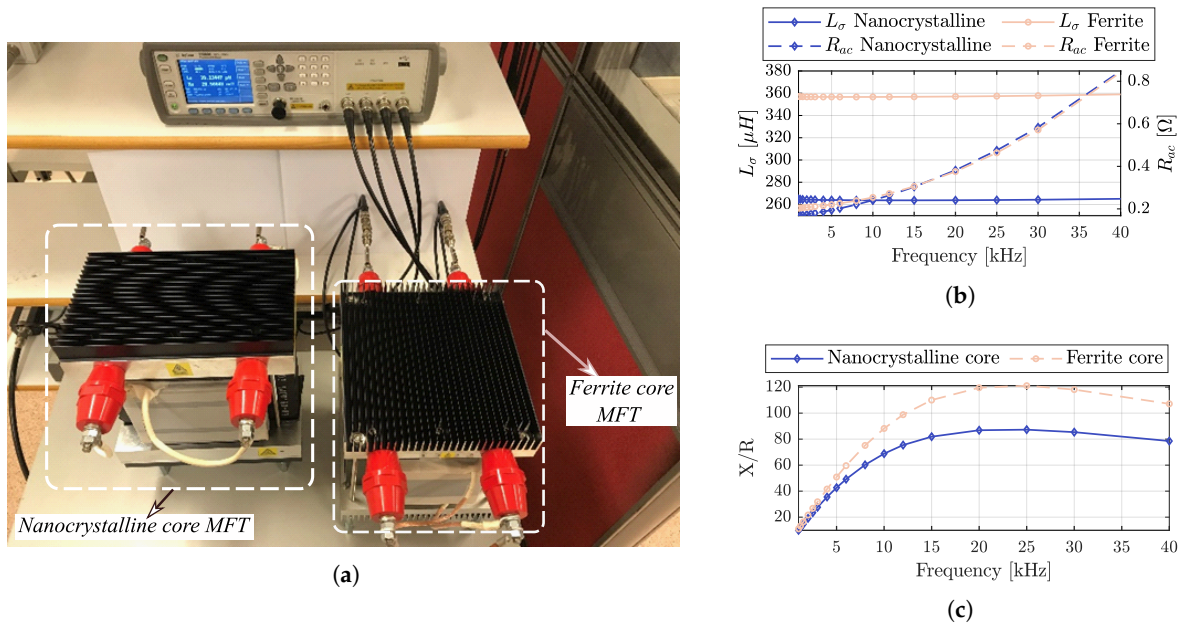


Figure 12. (a) Test setup for measuring the leakage inductance and the ac resistance of two MFTs. (b) The leakage inductance and ac resistance. (c) The ratio of the leakage reactance to the ac resistance.

In order to include the series ac resistance in the simulation, the first-order differential equation

$$L_{\sigma} \frac{dI_L(\omega t)}{dt} + R_{ac} I_L(\omega t) = v_{xN}(\omega t) - v'_{yn}(\omega t - \varphi) \quad (31)$$

should be solved while ensuring that $\bar{P}_{3\phi}(I_L(\omega t)) = P_n$ holds (for the 3 ϕ case). The initial condition for the current in (31) is unknown. Additionally, L_{σ} should be selected such that the RMS value of I_L is minimized for a certain range of variations in the amplitudes of $v_{xN}(\omega t)$ and $v'_{yn}(\omega t - \varphi)$. Overall, the problem becomes time-consuming to solve. Therefore, the simulation with the ac resistance is performed only for the 3 ϕ MFT and a single design where $(\sigma_p, \sigma_s) = (0.1, 0.1)$. The converter is assumed to have the same specifications as presented in Table 1. R_{ac} is varied such that the $\omega L_{\sigma}/R_{ac}$ ratio is kept close to or higher than the values shown in Figure 12c for a fundamental frequency of 5 kHz.

Figure 13 depicts the maximum of the currents in the operation domain as a function of leakage inductance for different $\omega L_{\sigma}/R_{ac}$ values obtained from the simulation model.

Here, $\omega L_\sigma / R_{ac} = \infty$ means that the ac resistance is neglected in the simulation. The current and the leakage inductance are normalized with respect to the case where $R_{ac} = 0$. When $\omega L_\sigma / R_{ac}$ reduces, the error in the $L_{\sigma,opt}$ value increases. For $\omega L_\sigma / R_{ac} = 43$, the value of $L_{\sigma,opt}$ is 4.8% higher compared with the case without resistance.

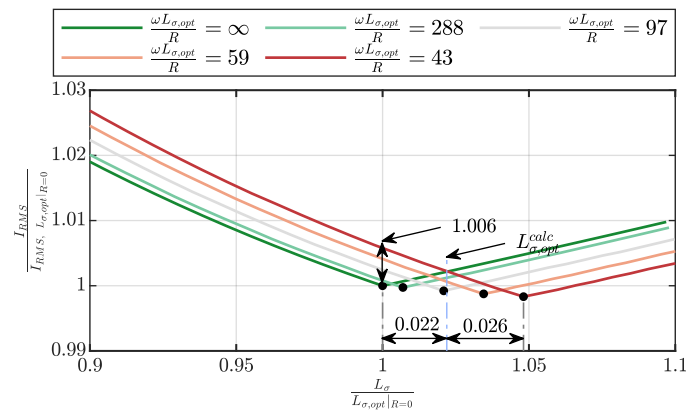


Figure 13. The maximum of the currents in the operation domain as a function of the leakage inductance for different $\omega L_\sigma / R_{ac}$ values obtained from the simulation model for $(\sigma_p, \sigma_s) = (0.1, 0.1)$. The dashed blue line marks the value of $L_{\sigma,opt}$ from the analytical formula ($L_{\sigma,opt}^{calc}$).

As seen, a 4.8% error in $L_{\sigma,opt}$ will cause a less than 1% error in the RMS value of the current. The value of $L_{\sigma,opt}$ from the analytical formula is depicted with a dashed blue line. The error between the $L_{\sigma,opt}^{calc}$ and $L_{\sigma,opt}^{sim}|_{R_{ac}=0}$ is 2.2%, which is the same value as shown in Figure 10a for $(\sigma_p, \sigma_s) = (0.1, 0.1)$.

5. Discussion

Analytical formulas are derived to estimate the desired leakage inductance value of the MFT for a DAB dc–dc converter. The estimated leakage inductance minimizes the RMS current for deviations in the dc-link voltages. This ensures minimum conduction losses under nominal power operation. The formulas are derived for converters with either single-phase or three-phase ac-links. They are independent of the converter topology and can be used for multilevel or conventional DAB converters.

The methods used in existing literature depend on solving optimization problems to determine leakage inductance. These methods are time-consuming and depend on an engineer with optimization-solving skills. On the other hand, the method proposed in this article uses a set of equations to determine the leakage inductance value (see Figure 7). This saves plenty of time for engineers interested in using the inductance value as an input to their MFT design optimization models.

The derived formulas are validated with MATLAB simulation models. It is shown that, in a broad design range, the error in the estimation of the leakage inductance can be less than 2.5% and 4% for the YY-connected three-phase MFT and the single-phase MFT, respectively. It is also highlighted that soft-switching can be ensured for specific converter designs using the presented equations (see Figure 6a).

The importance of selecting the leakage inductance correctly for a given voltage span is quantified. As an example, it is shown that for 11% deviations in the dc-link voltages, a 10% deviation from the desired leakage inductance value can cause 2% higher currents in the converter. In addition, the effect of neglecting the MFT's ac resistance on the leakage inductance's optimum value (and also the RMS current) is quantified. It is demonstrated that including an ac resistance close to its actual value in the optimization can cause a 5% difference in the value of the obtained optimum leakage inductance.

The main limitation of the proposed method is the high estimation error when a small deviation ($\sigma < 2\%$) is expected in only one of the dc-links (see Figure 11a). Moreover, it is

also shown that the estimation error is high for the $Y\Delta$ connection when deviations less than 10% in the dc-links are expected. This is attributed to the first harmonic approximation.

Improving the model's accuracy for the cases with a small deviation ($\sigma < 2\%$) in one of the dc-links can be valuable future work. Similarly, the accuracy of the model can be improved for the $Y\Delta$ connection of the windings and deviations less than 10% in the dc-links. Moreover, an interesting future study is using the leakage inductance of this paper as an input to the design and optimization of an MFT. Furthermore, evaluating the converter's performance at different applied voltages is suggested.

Author Contributions: Conceptualization, B.K., T.T.; methodology, B.K.; software, B.K.; validation, B.K. and M.K.; formal analysis, B.K.; investigation, B.K.; resources, T.T. and M.K.; data curation, B.K. and M.K.; writing—original draft preparation, B.K.; writing—review and editing, B.K., T.T. and M.K.; visualization, B.K.; supervision, T.T.; project administration, T.T.; funding acquisition, T.T. All authors have read and agreed to the published version of the manuscript.

Funding: This research is funded by Swedish Energy Agency (Energimyndigheten), Project No. 43048-1.

Data Availability Statement: Data sharing is not applicable to this article.

Acknowledgments: The authors gratefully acknowledge the financial support from the Swedish Energy Agency (Energimyndigheten). Also, the authors would like to thank Amin Bahmani for contributing to designing and developing the transformers.

Conflicts of Interest: The authors declare no conflict of interest. The funders had no role in the design of the study; in the collection, analyses, or interpretation of data; in the writing of the manuscript; or in the decision to publish the results.

Abbreviations

The following abbreviations are used in this manuscript:

DAB	Dual active bridge
RMS	Root mean square
MMC	Modular-multilevel converter
MFT	Medium-frequency transformer
Q2L	Quasi-two-level

Appendix A. Solving Optimization Problem (21)

Appendix A.1. Solving Inner Optimization

Problem (21) contains the sub-problem $\max_{U_p, U_s} (I_{LA,1}^{RMS})$, which should be solved first. If all of the local extrema of $I_{LA,1}^{RMS}$ are identified, the global maximum should be among these local extrema. Since the set \mathcal{R}_d is a convex set and $I_{LA,1}^{RMS}$ is a continuously differentiable function, the potential local maxima of $I_{LA,1}^{RMS}$ are the stationary points of the function. It will be shown here that all of the points in set \mathcal{R}_d except P_i where $i \in \{1, 2, 3, 4\}$ are either non-stationary or, if they are stationary points, they are not the global maximum.

A point in \mathcal{R}_d —excluding its vertices and edges—is stationary if $\nabla I_{LA,1}^{RMS} = 0$, where

$$\nabla I_{LA,1}^{RMS} = \left(\frac{\partial I_{LA,1}^{RMS}}{\partial U_p}, \frac{\partial I_{LA,1}^{RMS}}{\partial U_s} \right)^T. \quad (A1)$$

Solving $\nabla I_{LA,1}^{RMS} = 0$ results in $\pi^2 \omega L_\sigma P_n = 0$, which is an invalid expression. Therefore, $I_{LA,1}^{RMS}$ has no stationary point inside \mathcal{R}_d . For the edges, a point is stationary if the gradient

is perpendicular to the edge and pointing outwards from \mathcal{R}_d . For the edges parallel with the U_s -axis, this means

$$\frac{\partial I_{LA,1}^{\text{RMS}}}{\partial U_s} = 0 \Rightarrow U_{s1} = \sqrt{U_{p1}^2 + \left(\frac{\pi^2 \omega L_\sigma P_n}{24 U_{p1}}\right)^2} \Rightarrow \frac{\partial I_{LA,1}^{\text{RMS}}}{\partial U_p} < 0. \quad (\text{A2})$$

This means that there are no stationary points on the edge connecting vertices P_3 and P_4 , whereas for a given L_σ , there is a single stationary point on the edge connecting vertices P_1 and P_2 . For a given L_σ , comparing the value of the current on P_2 with the value of the current on this stationary point reveals that the current value in point P_2 is higher irrespective of the L_σ value. Therefore, there are no stationary points with the potential of being the global maximum on the edges parallel to the U_s -axis. With a similar approach, it can be shown that there are no stationary points with the potential of being the global maximum on the edges parallel to the U_p -axis. Finally, the only points with the potential to be the global maximum are the points P_i where $i \in \{1, 2, 3, 4\}$.

Appendix A.2. Solving Outer Optimization

It is shown that the potential extrema of $I_{LA,1}^{\text{RMS}}$ subject to constraint (16) are points P_i where $i \in \{1, 2, 3, 4\}$ (see Figure 5). Therefore, the value of L_σ that minimizes the maximum value of $I_{LA,1}^{\text{RMS}}$ on points P_i is the solution to the problem (21). For clarification, Figure A1 shows the phase currents of the MFT on the points P_i as a function of the leakage inductance. The dashed green curve is the maximum of the currents on the operation domain (shown in Figure 5). The value of L_σ that minimizes this curve will ensure that the phase currents in the whole operation domain will be kept to their minimum possible values. To solve (21), the intersections of the currents at the points P_i and P_j where $\{i, j\} \in \{1, 2, 3, 4\}$ and $i \neq j$ are identified. Subsequently, an analytical expression is derived at each identified interval. The total number of intersections is equal to the number of 2-combinations of $\{P_1, P_2, P_3, P_4\}$, which is six.

To get a comprehensible analytical expression for the leakage inductance, it is assumed that $U_{1,p,M} \approx U_{1,s,M}$ where $U_{1,p,M}$ and $U_{1,s,M}$ are given in (22). Solving either $I_{LA,1}^{\text{RMS}}|_{P_1} = I_{LA,1}^{\text{RMS}}|_{P_4}$ or $I_{LA,1}^{\text{RMS}}|_{P_3} = I_{LA,1}^{\text{RMS}}|_{P_4}$ results in an invalid expression, meaning that there is no real-valued L_σ satisfying these equations. Similarly, solving $I_{LA,1}^{\text{RMS}}|_{P_2} = I_{LA,1}^{\text{RMS}}|_{P_4}$ will result in $L_\sigma = 0$. This means that there is no $L_\sigma \in \mathbb{R}^+$ where the currents in the points $\{P_1, P_2, P_3\}$ intersect with the current in the point P_4 . These can also be seen in Figure A1 where there is no intersection of currents for these points. Likewise, $I_{LA,1}^{\text{RMS}}|_{P_1} = I_{LA,1}^{\text{RMS}}|_{P_3}$ results in an unacceptable solution. On the other hand, there exists $L_\sigma \in \mathbb{R}^+$ such that $I_{LA,1}^{\text{RMS}}|_{P_1} = I_{LA,1}^{\text{RMS}}|_{P_2}$ or $I_{LA,1}^{\text{RMS}}|_{P_3} = I_{LA,1}^{\text{RMS}}|_{P_2}$. $L_{\sigma,\text{opt}}$ is calculated by solving these two equations and identifying the regions where each solution is valid.

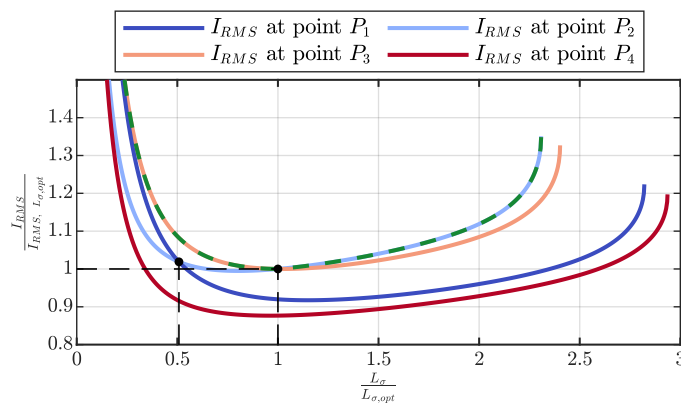


Figure A1. The phase currents of the MFT on the points P_i , $i \in \{1, 2, 3, 4\}$ as a function of the leakage inductance. The dashed green curve shows the maximum of the currents on the operation domain.

References

- De Doncker, R.; Divan, D.; Kheraluwala, M. A three-phase soft-switched high-power-density DC/DC converter for high-power applications. *IEEE Trans. Ind. Appl.* **1991**, *27*, 63–73. [\[CrossRef\]](#)
- Páez, J.D.; Frey, D.; Maneiro, J.; Bacha, S.; Dworakowski, P. Overview of DC–DC Converters Dedicated to HVDC Grids. *IEEE Trans. Power Deliv.* **2019**, *34*, 119–128. [\[CrossRef\]](#)
- She, X.; Huang, A.Q.; Burgos, R. Review of Solid-State Transformer Technologies and Their Application in Power Distribution Systems. *IEEE J. Emerg. Sel. Top. Power Electron.* **2013**, *1*, 186–198. [\[CrossRef\]](#)
- Bahmani, M.A.; Vechalapu, K.; Mobarrez, M.; Bhattacharya, S. Flexible HF distribution transformers for inter-connection between MVAC and LVDC connected to DC microgrids: Main challenges. In Proceedings of the 2017 IEEE Second International Conference on DC Microgrids (ICDCM), Nuremberg, Germany, 27–29 June 2017; pp. 53–60. [\[CrossRef\]](#)
- Adam, G.P.; Gowaid, I.A.; Finney, S.J.; Holliday, D.; Williams, B.W. Review of Dc–Dc Converters for Multi-Terminal HVDC Transmission Networks. *IET Power Electron.* **2016**, *9*, 281–296. [\[CrossRef\]](#)
- Xing, Z.; Ruan, X.; You, H.; Yang, X.; Yao, D.; Yuan, C. Soft-Switching Operation of Isolated Modular DC/DC Converters for Application in HVDC Grids. *IEEE Trans. Power Electron.* **2016**, *31*, 2753–2766. [\[CrossRef\]](#)
- Baars, N.H.; Wijnands, C.G.E.; Everts, J. ZVS modulation strategy for a three-phase dual active bridge dc-dc converter with three-level phase-legs. In Proceedings of the 2016 18th European Conference on Power Electronics and Applications (EPE'16 ECCE Europe), Karlsruhe, Germany, 5–9 September 2016; pp. 1–10. [\[CrossRef\]](#)
- Filba-Martinez, A.; Busquets-Monge, S.; Bordonau, J. Modulation and Capacitor Voltage Balancing Control of Multilevel NPC Dual Active Bridge DC–DC Converters. *IEEE Trans. Ind. Electron.* **2020**, *67*, 2499–2510. [\[CrossRef\]](#)
- Gowaid, I.A.; Adam, G.P.; Massoud, A.M.; Ahmed, S.; Williams, B.W. Hybrid and Modular Multilevel Converter Designs for Isolated HVDC–DC Converters. *IEEE J. Emerg. Sel. Top. Power Electron.* **2018**, *6*, 188–202. [\[CrossRef\]](#)
- Gowaid, I.A.; Adam, G.P.; Massoud, A.M.; Ahmed, S.; Holliday, D.; Williams, B.W. Quasi Two-Level Operation of Modular Multilevel Converter for Use in a High-Power DC Transformer With DC Fault Isolation Capability. *IEEE Trans. Power Electron.* **2015**, *30*, 108–123. [\[CrossRef\]](#)
- Gowaid, I.A.; Adam, G.P.; Ahmed, S.; Holliday, D.; Williams, B.W. Analysis and Design of a Modular Multilevel Converter with Trapezoidal Modulation for Medium and High Voltage dc-dc Transformers. *IEEE Trans. Power Electron.* **2015**, *30*, 5439–5457. [\[CrossRef\]](#)
- Khanzadeh, B.; Thiringer, T.; Okazaki, Y. Capacitor Size Comparison on High-Power dc-dc Converters with Different Transformer Winding Configurations on the AC-link. In Proceedings of the 2020 22nd European Conference on Power Electronics and Applications (EPE'20 ECCE Europe), Lyon, France, 7–11 September 2020; pp. P.1–P.7. [\[CrossRef\]](#)
- Khanzadeh, B.; Okazaki, Y.; Thiringer, T. Capacitor and Switch Size Comparisons on High-Power Medium-Voltage DC–DC Converters With Three-Phase Medium-Frequency Transformer. *IEEE J. Emerg. Sel. Top. Power Electron.* **2021**, *9*, 3331–3338. [\[CrossRef\]](#)
- Burkart, R.M.; Kolar, J.W. Comparative η – ρ – σ Pareto Optimization of Si and SiC Multilevel Dual-Active-Bridge Topologies With Wide Input Voltage Range. *IEEE Trans. Power Electron.* **2017**, *32*, 5258–5270. [\[CrossRef\]](#)
- Bahmani, M.A.; Thiringer, T. Accurate Evaluation of Leakage Inductance in High-Frequency Transformers Using an Improved Frequency-Dependent Expression. *IEEE Trans. Power Electron.* **2015**, *30*, 5738–5745. [\[CrossRef\]](#)
- Bahmani, M.A.; Thiringer, T.; Rabiei, A.; Abdulahovic, T. Comparative Study of a Multi-MW High-Power Density DC Transformer With an Optimized High-Frequency Magnetics in All-DC Offshore Wind Farm. *IEEE Trans. Power Deliv.* **2016**, *31*, 857–866. [\[CrossRef\]](#)
- Bahmani, M.A.; Thiringer, T.; Kharezy, M. Design Methodology and Optimization of a Medium-Frequency Transformer for High-Power DC–DC Applications. *IEEE Trans. Ind. Appl.* **2016**, *52*, 4225–4233. [\[CrossRef\]](#)

18. Eslamian, M.; Kharezy, M.; Thiringer, T. Calculation of the Leakage Inductance of Medium Frequency Transformers with Rectangular-Shaped Windings using an Accurate Analytical Method. In Proceedings of the 2019 21st European Conference on Power Electronics and Applications (EPE '19 ECCE Europe), Genova, Italy, 3–5 September 2019; pp. P.1–P.10. [[CrossRef](#)]
19. Bin, C. Design optimisation of an inductor-integrated MF transformer for a high-power isolated dual-active-bridge DC–DC converter. *IET Power Electron.* **2019**, *12*, 2912–2922. [[CrossRef](#)]
20. Chen, B.; Liang, X.; Wan, N. Design Methodology for Inductor-Integrated Litz-Wired High-Power Medium-Frequency Transformer With the Nanocrystalline Core Material for Isolated DC-Link Stage of Solid-State Transformer. *IEEE Trans. Power Electron.* **2020**, *35*, 11557–11573. [[CrossRef](#)]
21. Garcia-Bediaga, A.; Villar, I.; Rujas, A.; Mir, L.; Rufer, A. Multiobjective Optimization of Medium-Frequency Transformers for Isolated Soft-Switching Converters Using a Genetic Algorithm. *IEEE Trans. Power Electron.* **2017**, *32*, 2995–3006. [[CrossRef](#)]
22. Zhang, X.; Xiao, F.; Wang, R.; Kang, W.; Yang, B. Modeling and Design of High-Power Enhanced Leakage-Inductance-Integrated Medium-Frequency Transformers for DAB Converters. *Energies* **2022**, *15*, 1361. [[CrossRef](#)]
23. Yazdani, F.; Zolghadri, M. Design of dual active bridge isolated bi-directional DC converter based on current stress optimization. In Proceedings of the 2017 8th Power Electronics, Drive Systems & Technologies Conference (PEDSTC), Mashhad, Iran, 14–16 February 2017; pp. 247–252. [[CrossRef](#)]
24. D'Antonio, M.; Chakraborty, S.; Khaligh, A. Design Optimization for Weighted Conduction Loss Minimization in a Dual-Active-Bridge-Based PV Microinverter. In Proceedings of the 2020 IEEE Energy Conversion Congress and Exposition (ECCE), Washington, DC, USA, 11–15 October 2020; pp. 6008–6015. [[CrossRef](#)]
25. Siebke, K.; Giacomazzo, M.; Mallwitz, R. Design of a Dual Active Bridge Converter for On-Board Vehicle Chargers using GaN and into Transformer Integrated Series Inductance. In Proceedings of the 2020 22nd European Conference on Power Electronics and Applications (EPE'20 ECCE Europe), Lyon, France, 7–11 September 2020; pp. 1–8. [[CrossRef](#)]
26. Nguyen, H.V.; To, D.D.; Lee, D.C. Onboard battery chargers for plug-in electric vehicles with dual functional circuit for low-voltage battery charging and active power decoupling. *IEEE Access* **2018**, *6*, 70212–70222. [[CrossRef](#)]
27. Lenke, R.U. *A Contribution to the Design of Isolated DC-DC Converters for Utility Applications*; E.ON Energy Research Center, RWTH Aachen University: Aachen, Germany, 2012.
28. Krismer, F.; Round, S.; Kolar, J.W. Performance optimization of a high current dual active bridge with a wide operating voltage range. In Proceedings of the 2006 37th IEEE Power Electronics Specialists Conference, Jeju, Republic of Korea, 18–22 June 2006; pp. 1–7. [[CrossRef](#)]
29. van Hoek, H.; Neubert, M.; De Doncker, R.W. Enhanced Modulation Strategy for a Three-Phase Dual Active Bridge—Boosting Efficiency of an Electric Vehicle Converter. *IEEE Trans. Power Electron.* **2013**, *28*, 5499–5507. [[CrossRef](#)]
30. Hoang, K.D.; Wang, J. Design optimization of high frequency transformer for dual active bridge dc-dc converter. In Proceedings of the 2012 XXth International Conference on Electrical Machines, Marseille, France, 2–5 September 2012; pp. 2311–2317. [[CrossRef](#)]
31. Alikhanzadeh, B.; Thiringer, T.; Kharezy, M. Optimum Leakage Inductance Determination for a Q2L-Operating MMC-DAB with Different Transformer Winding Configurations. In Proceedings of the 2019 20th International Symposium on Power Electronics (Ee), Novi Sad, Serbia, 23–26 October 2019; pp. 1–6. [[CrossRef](#)]
32. O'neil, P.V. *Advanced Engineering Mathematics*; Cengage Learning: Boston, MA, USA, 2017.
33. Lovelock, D.; Rund, H. *Tensors, Differential Forms, and Variational Principles*; Courier Corporation: Chelmsford, MA, USA, 1989.
34. Svoboda, J.A.; Dorf, R.C. *Introduction to Electric Circuits*; John Wiley & Sons: Hoboken, NJ, USA, 2013.
35. Khanzadeh, B.; Thiringer, T.; Serdyuk, Y. Analysis and Improvement of Harmonic Content in Multi-level Three-phase DAB Converters with Different Transformer Windings Connections. In Proceedings of the 2022 International Power Electronics Conference (IPEC-Himeji 2022- ECCE Asia), Himeji, Japan, 15–19 May 2022; pp. 2653–2658. [[CrossRef](#)]
36. Bahmani, A. *Design and Optimization Considerations of Medium-Frequency Power Transformers in High-Power DC-DC Applications*; Chalmers Tekniska Hogskola: Göteborg, Sweden, 2016.

Disclaimer/Publisher's Note: The statements, opinions and data contained in all publications are solely those of the individual author(s) and contributor(s) and not of MDPI and/or the editor(s). MDPI and/or the editor(s) disclaim responsibility for any injury to people or property resulting from any ideas, methods, instructions or products referred to in the content.